



# Highly photocatalytic active thiomolybdate $[\text{Mo}_3\text{S}_{13}]^{2-}$ clusters/BiOBr nanocomposite with enhanced sulfur tolerance



Dongting Yue, Taiyang Zhang, Miao Kan, Xufang Qian, Yixin Zhao \*

School of Environmental Science and Engineering, Shanghai Jiao Tong University, 800 Dongchuan Rd., Shanghai 200240, China

## ARTICLE INFO

### Article history:

Received 11 August 2015

Received in revised form 6 October 2015

Accepted 11 October 2015

Available online 23 October 2015

### Keywords:

Photocatalyst

$\text{Mo}_3\text{S}_{13}^{2-}$ /BiOBr

$[\text{Mo}_3\text{S}_{13}]^{2-}$  nanoclusters

Sulfur tolerant

## ABSTRACT

The sulfur tolerant  $\text{Mo}_3\text{S}_{13}^{2-}$ /BiOBr nanocomposite photocatalysts were facilely fabricated by a hydrothermal method. The characterizations including X-ray photoelectron spectroscopy (XPS), X-ray diffraction (XRD), scanning electron microscopy (SEM), transmission electron microscopy (TEM), energy dispersive X-ray spectrometry (EDS), UV–vis diffuse reflection spectroscopy (DRS) and photoluminescence (PL) investigate the structures, elemental composition, morphologies and photocatalytic activities of  $\text{Mo}_3\text{S}_{13}^{2-}$ /BiOBr nanocomposite. The 5.0 wt%  $\text{Mo}_3\text{S}_{13}^{2-}$ /BiOBr composite sample showed highest visible-light-driven photocatalytic activity for decolorization of organic dyes including Rhodamine B (RhB) and sulfur containing methylene blue (MB). The decolorization of RhB was dominated by the direct hole and the generated  $\cdot\text{O}_2^-$  radicals oxidation process. Our 5.0 wt%  $\text{Mo}_3\text{S}_{13}^{2-}$ /BiOBr nanocomposite exhibited comparable photocatalytic activity as the state of art 1 wt% BiOBr/Pt composite for photocatalytic decolorization of RhB. The 5.0 wt%  $\text{Mo}_3\text{S}_{13}^{2-}$ /BiOBr composite possessed better sulfur resistance than 1.0 wt% Pt/BiOBr composite.

© 2015 Elsevier B.V. All rights reserved.

## 1. Introduction

Semiconductor photocatalysis technique, a “green” method for environmental remediation and the conversion of solar energy into chemical energy, has attracted tremendous research attention [1–3]. Unfortunately, the classical and most widely used photocatalysts of  $\text{TiO}_2$  can only utilize the UV light, which covers only 4% of the whole solar spectrum. Many different techniques and novel photocatalysts have been developed to extend their activities to the visible light. Recently, an important class of ternary compounds of bismuth oxyhalides ( $\text{BiOX}$ ,  $\text{X}=\text{Cl}$ ,  $\text{Br}$ ,  $\text{I}$ ) have been widely investigated due to their excellent visible light photocatalytic activities [4–14]. Among these  $\text{BiOX}$  photocatalysts, BiOBr is of great research interest owing to its stability, suitable band gap and superior photocatalytic abilities. BiOBr has a layered structure of  $[\text{Bi}_2\text{O}_2]$  slabs intercalated with double slabs of bromine atoms. Furthermore, BiOBr possesses indirect-transition band-gap (2.75 eV), leading to a better photocatalytic oxidation and reduction performance under visible light irradiation due to its longer lifetime charge carriers [4,15–17]. Until now, BiOBr has been widely utilized in photocatalytic applications such as photodegradation of

dyes, nitrogen oxide and microcystin-LR [6,12,18,19], and so many different methods have been reported to prepare various BiOBr micro/nanostructures [20–27]. Co-catalyst is another most popular approach to enhance photocatalysts’ activities by promote charge separation and charge transfer. Platinum and other noble metals are widely adopted as co-catalyst for enhancing photocatalysis due to their high activities with negligible overpotential even under high reaction rates. However, the scarcity and high cost of noble metals especially platinum limit their large scale application [28]. In addition, industrial wastewater from the dye industry usually contain considerable amounts of sulfur compound such as  $\text{S}^{2-}$  which tends to poison these noble metal co-catalysts especially platinum.

Recently, molybdenum sulfide materials ( $\text{MoS}_x$ ) have emerged as one of most of popular low-cost, earth-abundant alternatives to Pt and other noble metals for their unique electronic and chemical properties [29]. The small  $[\text{Mo}_3\text{S}_{13}]^{2-}$  nanoclusters, reported by Kibsgaard et al. [28], inherently expose a significant number of active edge sites. The enhanced catalytic activity of the  $[\text{Mo}_3\text{S}_{13}]^{2-}$  clusters complex is attributed to their three different types of sulfur ligands, which locate intrinsically as edge sulfur atoms. Such unique structure could potentially enable  $[\text{Mo}_3\text{S}_{13}]^{2-}$ -based catalysts comparable to the best precious-metal catalysts such as platinum [28]. Besides, previous reports have demonstrate its excellent stability when used as electrocatalysts and co-catalyst [28,30–32]. In this report, we prepared the  $\text{Mo}_3\text{S}_{13}^{2-}$ /BiOBr

\* Corresponding author.

E-mail address: [yixin.zhao@sjtu.edu.cn](mailto:yixin.zhao@sjtu.edu.cn) (Y. Zhao).

nanocomposites via a facile hydro-thermal method. We investigate the photodegradation of RhB under visible light irradiation catalyzed by our  $\text{Mo}_3\text{S}_{13}^{2-}/\text{BiOBr}$  nanocomposites in a sulfur-containing dye wastewater. The  $[\text{Mo}_3\text{S}_{13}]^{2-}$  clusters prove to be a highly active and low-cost co-catalyst for BiOBr, which not only exhibit enhanced photocatalytic activity comparable to Pt but also showed much better sulfur tolerance. A photocatalytic mechanism for the  $\text{Mo}_3\text{S}_{13}^{2-}/\text{BiOBr}$  composites is also discussed.

## 2. Experimental

### 2.1. Chemicals

$\text{TiO}_2$  powders (Degussa P25, ca. 80% anatase) were used as received. Bismuth(III) nitrate pentahydrate, ethylenediamine tetraacetic acid disodium salt dihydrate (EDTA-2Na), *tert*-butanol (TBA), Rhodamine B (RhB), ammonium heptamolybdate tetrahydrate ( $(\text{NH}_4)_6\text{Mo}_7\text{O}_{24}\cdot 4\text{H}_2\text{O}$ ), chloroplatinic acid hexahydrate, carbon disulfide, toluene and ethanol were of analytical purity and were used as received. All of them were purchased from Sinopharm Chemical Reagent Co., Ltd. Cetyltrimethylammonium bromide (CTAB) and barium sulfate were purchased from Aladdin Industrial Corporation. Ammonium polysulfide solution was purchased from Xiya reagent.

### 2.2. Materials synthesis

#### 2.2.1. Synthesis of $[\text{Mo}_3\text{S}_{13}]^{2-}$ nanoclusters

The thiomolybdate  $(\text{NH}_4)_2\text{Mo}_3\text{S}_{13}\cdot n\text{H}_2\text{O}$  ( $n=0-2$ ) was prepared according to Kibsgaard et al. [28]. A 4.0 g of  $(\text{NH}_4)_6\text{Mo}_7\text{O}_{24}\cdot 4\text{H}_2\text{O}$  was dissolved in 20 mL of water in an Erlenmeyer flask. An ammonium polysulfide solution was added and the flask was covered with a watch glass. The solution was then kept on an oil bath ( $96^\circ\text{C}$ ) for five days without stirring. Dark-red crystals of  $(\text{NH}_4)_2\text{Mo}_3\text{S}_{13}\cdot n\text{H}_2\text{O}$  precipitated and the obtained samples were centrifuged and washed three times with distilled water and ethanol. In order to remove excess sulfur, the  $(\text{NH}_4)_2\text{Mo}_3\text{S}_{13}\cdot n\text{H}_2\text{O}$  crystals were heated in hot toluene ( $80^\circ\text{C}$ ) for 3 h. Finally, the crystals were dried in air.

#### 2.2.2. The preparation of $\text{Mo}_3\text{S}_{13}^{2-}/\text{BiOBr}$ and $\text{Pt}/\text{BiOBr}$

1.0 mmol  $\text{Bi}(\text{NO}_3)_3\cdot 5\text{H}_2\text{O}$  and 2.2 mmol of cetyltrimethylammonium bromide (CTAB) were added into a 50 mL beaker, and then 20 mL deionized water and 1 mL ethanol were added followed by stirring for 20 min. Different amounts of  $(\text{NH}_4)_2\text{Mo}_3\text{S}_{13}$  solution were added into the mixture solution and stirred for 10 min, then the solution was transferred into a 25 mL Teflon-lined autoclave and heated at  $140^\circ\text{C}$  for 18 h. The obtained samples were centrifuged and washed three times with distilled water and ethanol. Finally, the samples were dried at  $60^\circ\text{C}$  for 4 h before further characterization. The weight contents of  $(\text{NH}_4)_2\text{Mo}_3\text{S}_{13}$  in the composite photocatalysts were 1 wt%, 3 wt%, 5 wt% and 6.5 wt%. For comparison, pure BiOBr was synthesized using the similar processes and 1 wt% Pt/BiOBr composite were synthesized according to the previous report [33]. 1 wt% Pt/ $\text{TiO}_2$  and 5 wt%  $\text{Mo}_3\text{S}_{13}^{2-}/\text{TiO}_2$  was also prepared according to previous reports [34].

### 2.3. Characterization

The crystal structures of the samples were characterized by X-ray diffraction (XRD) on a Bruker D8 Advance X-ray diffractometer with Cu-K $\alpha$  radiation ( $\lambda = 1.54 \text{ \AA}$ ) at 40 kV and 40 mA. The data were recorded at a scan rate of  $10^\circ \text{ min}^{-1}$  in the  $2\theta$  range from  $10^\circ$  to  $80^\circ$ . The morphologies of  $\text{Mo}_3\text{S}_{13}^{2-}/\text{BiOBr}$  nanocomposites were carried out on a field-emission scanning electron

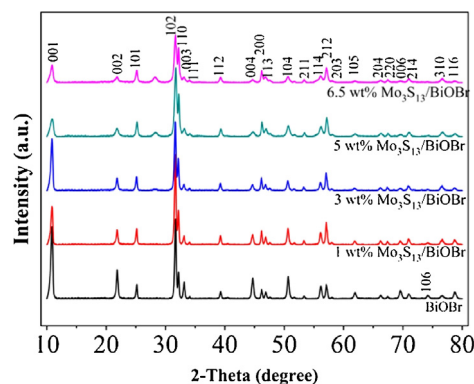


**Fig. 1.** XRD patterns of BiOBr and  $\text{Mo}_3\text{S}_{13}^{2-}/\text{BiOBr}$  composites with different mass ratios of  $[\text{Mo}_3\text{S}_{13}]^{2-}$ .

microscope equipped with an energy-dispersive X-ray spectroscopy (EDS) operating at an acceleration voltage of 25 kV (FEI & Oxford Sirion 200 & INCA X-Act). The elemental composition of samples were determined by inductively coupled plasma optical emission spectrometer (ICP-AES, iCAP 6300, Thermo, USA). The surface analysis was investigated by X-ray photoelectron spectroscopy (XPS, Kratos Axis Ultra DLD), and the spectra calibrated to the C 1s peak at 284.6 eV. Transmission electron microscopy (TEM) micrographs were obtained using a JEOL-JEM-2010 microscope (JEOL, Japan) operating at 200 kV. Diffuse reflectance spectra (DRS) were measured in the range of 200–800 nm using a UV-vis spectrophotometer (Shimadzu UV-2450, Japan).  $\text{BaSO}_4$  was used as the reflectance standard material. Photoluminescence (PL) measurements of the  $\text{Mo}_3\text{S}_{13}^{2-}/\text{BiOBr}$  composites were carried out using an excitation wavelength of 360 nm by fluorescence spectrophotometer (F-380, Tianjin Gangdong SCI. & TECH. Development Co., Ltd.). The slit width for the measurements was 10 nm. Powder samples were used without further treatment.

### 2.4. Photocatalytic activity evaluation

The visible light ( $\lambda \geq 420 \text{ nm}$ ) photocatalytic activities of the composite powders were evaluated by the degradation of RhB and MB using a 150 W Halogen lamp (Cealight, CEL-TCH150) as the light source. 0.02 g photocatalysts were added into 50 mL RhB solution with a concentration 10 mg/L in the photocatalysis reactor. For the degradation of 5 mg/L MB solution, 0.05 g photocatalysts were added into 50 mL MB solution. Prior to irradiation, the solution was stirred for 30 min in the dark to reach the adsorption-desorption equilibrium of organic dyes (RhB and MB) on the surface of samples. During irradiation, approximately 3 mL of the suspension was taken periodically at different time interval, and then the photocatalyst powder and the solution were separated from solution by centrifugation. The concentration of RhB and MB was analyzed under its characteristic absorption wavelength of 553 and 664 nm on a UV-vis spectrophotometer (Agilent Cary 60, Agilent). For the regeneration test of the photocatalyst, 5 consecutive cycles of MB were tested, and the samples were washed thoroughly with DI water and dried after each cycle.

## 3. Results and discussion

Through a facile hydrothermal route, the assembled BiOBr nanosheets and the  $\text{Mo}_3\text{S}_{13}^{2-}/\text{BiOBr}$  composites with different mass ratios were synthesized. Fig. 1 shows the XRD patterns of BiOBr and the  $\text{Mo}_3\text{S}_{13}^{2-}/\text{BiOBr}$  composites with different mass ratios. XRD pattern (Fig. 1) reveals that all these samples have the characteristic diffraction peaks attributing to tetragonal BiOBr

(JCPDS No. 09-0393) with the most intensive diffraction peak of (102). The as-synthesized  $\text{Mo}_3\text{S}_{13}^{2-}/\text{BiOBr}$  nanocomposites also have the dominant (102) diffraction peaks (Fig. 1), implying their preferred orientations along the (102) plane [35]. Since the  $(\text{NH}_4)_2\text{Mo}_3\text{S}_{13} \cdot n\text{H}_2\text{O}$  has weak XRD pattern compared to BiOBr as listed in Fig. S1, which is in agreement with the simulated powder XRD patterns of  $(\text{NH}_4)_2\text{Mo}_3\text{S}_{13} \cdot n\text{H}_2\text{O}$  (JCPDS 76-2038) [28,36]. There is no obvious XRD signal assigned to  $[\text{Mo}_3\text{S}_{13}]^{2-}$  clusters in these  $\text{Mo}_3\text{S}_{13}^{2-}/\text{BiOBr}$  composites.

The morphologies of BiOBr and 5 wt%  $\text{Mo}_3\text{S}_{13}^{2-}/\text{BiOBr}$  composites were investigated by SEM and TEM. The typical SEM images in Fig. 2(a) and (b) showed that the samples were composed of assembled nanosheets, and the pure BiOBr and 5 wt%  $\text{Mo}_3\text{S}_{13}^{2-}/\text{BiOBr}$  composites has no change in morphologies. It indicated that the addition of  $[\text{Mo}_3\text{S}_{13}]^{2-}$  would not affect the morphologies of assembled BiOBr nanosheets. As indicated in Fig 2(c) and (d), the fringe spacing of 0.172 nm agrees well with that of the (2 1 1) lattice planes (0.171 nm) of the 5 wt%  $\text{Mo}_3\text{S}_{13}^{2-}/\text{BiOBr}$  composites. Therefore, the 5 wt%  $\text{Mo}_3\text{S}_{13}^{2-}/\text{BiOBr}$  sample has predominantly exposed (102) facets, which is consistent with the XRD in Fig. 1. High resolution TEM (HRTEM) image of  $[\text{Mo}_3\text{S}_{13}]^{2-}$  clusters is shown in Fig. 2(e). Since the  $[\text{Mo}_3\text{S}_{13}]^{2-}$  cluster particles size is less than 15 nm and the contrast of  $[\text{Mo}_3\text{S}_{13}]^{2-}$  clusters and BiOBr is low, it is difficult to observe the  $[\text{Mo}_3\text{S}_{13}]^{2-}$  clusters on the surface of BiOBr by SEM as shown in Fig. 2(b). However, the EDS pattern (Fig. 2(f)) confirmed that the 5 wt%  $\text{Mo}_3\text{S}_{13}^{2-}/\text{BiOBr}$  composite contained O, Br, Mo, S and Bi elements, which is also consistent with the ICP element analysis (Table S1).

XPS analysis was carried out to analyze the chemical composition and elucidate the chemical state of the BiOBr and  $\text{Mo}_3\text{S}_{13}^{2-}/\text{BiOBr}$  composite (Fig. 3). The high-resolution Bi 4f spectrum of the pure BiOBr exhibits two peaks at 159.4 eV and 164.41 eV, which are characteristic of the  $\text{Bi}^{3+}$  in the  $\text{Mo}_3\text{S}_{13}^{2-}/\text{BiOBr}$  composite (Fig. 3(a)). However, the peaks Bi 4f<sub>7/2</sub> and Bi 4f<sub>5/2</sub> for  $\text{Mo}_3\text{S}_{13}^{2-}/\text{BiOBr}$  composite at 159.08 and 164.20 eV are lower than those of pure BiOBr. The Br 3d and O 1s XPS spectra could be observed at binding energies of 68.95 eV and 529.98 eV corresponding to Br and O in BiOBr. The peak positions were shifted when BiOBr was hybridized by  $[\text{Mo}_3\text{S}_{13}]^{2-}$ . These results imply the interactions between the  $\text{Mo}_3\text{S}_{13}^{2-}$  and BiOBr, not a simply physical adsorption. Deconvolution of the Mo 3d region by peak fitting indicated a single Mo 3d doublet at a position indicative of Mo with a 4+ oxidation state. The feature of S 2s was obtained near the Mo 3d<sub>5/2</sub> peak, which revealed multiple chemical states of sulfur (Fig. 3(d)) [28].

The optical absorbance of pure BiOBr and the  $\text{Mo}_3\text{S}_{13}^{2-}/\text{BiOBr}$  composites were determined by a UV–vis diffuse reflectance spectra (DRS). As shown in Fig. 4(a), the pure BiOBr sample showed a characteristic absorption edge at 435 nm which was quite consistent with the previous reported BiOBr [35]. As shown in Fig. S2, the  $[\text{Mo}_3\text{S}_{13}]^{2-}$  nanocluster exhibited absorbance in visible light region, which is up to 600 nm. As a result, the reflectance of the  $[\text{Mo}_3\text{S}_{13}]^{2-}/\text{BiOBr}$  composites was gradually red shifted compared with pure BiOBr due to the coupling of these brown  $[\text{Mo}_3\text{S}_{13}]^{2-}$  nanocluster onto BiOBr. The generation of electron/hole pairs, as well as their separation, migration and trapping by the reactive species, is identified as one of most important fundamental step for the photocatalysts. Photoluminescence (PL) spectra is a well known technique to investigate the efficiency of charge capture and recombination of photogenerated electron/hole pairs in a semiconductor. PL spectra of the pure BiOBr and  $\text{Mo}_3\text{S}_{13}^{2-}/\text{BiOBr}$  samples excited with 360 nm are listed in Fig. 4(b). The PL intensities of the  $\text{Mo}_3\text{S}_{13}^{2-}/\text{BiOBr}$  samples decrease with  $[\text{Mo}_3\text{S}_{13}]^{2-}$  content, which implied that the  $[\text{Mo}_3\text{S}_{13}]^{2-}$  effectively quench the BiOBr in the  $\text{Mo}_3\text{S}_{13}^{2-}/\text{BiOBr}$  [37–39]. In other words, the separation

efficiency of photogenerated electrons and holes in 5 wt% and 6.5 wt%  $\text{Mo}_3\text{S}_{13}^{2-}/\text{BiOBr}$  composites is higher than others.

The photocatalytic performance of pure BiOBr and  $\text{Mo}_3\text{S}_{13}^{2-}/\text{BiOBr}$  composites were evaluated by the decolorization of RhB under visible light irradiation, as shown in Fig. 5(a). The variation of the time-dependent absorption spectra of RhB solution in the presence of 5 wt%  $\text{Mo}_3\text{S}_{13}^{2-}/\text{BiOBr}$  sample is shown in Fig. S3. The intensity of the peak at 553 nm decreased significantly as the exposure time increased, accompanied by a shift in the absorption band towards the blue region. The blue-shift can be ascribed to the step-by-step deethylation process [27]. After 180 min irradiation, both the maximum absorption peak and absorption at 553 nm disappeared, which indicated that RhB could be completely decolorized by using 5 wt%  $\text{Mo}_3\text{S}_{13}^{2-}/\text{BiOBr}$  sample. The self-photolysis of RhB dye without catalyst under visible light irradiation was not observable, which indicated that its self-photolysis is negligible. More than 75% of RhB was decolorized by pure BiOBr after 50 min of visible light irradiation. The photocatalytic activity of  $\text{Mo}_3\text{S}_{13}^{2-}/\text{BiOBr}$  composites is enhanced with increase of  $[\text{Mo}_3\text{S}_{13}]^{2-}$  clusters content from 1 wt% to 5 wt%, in which the  $[\text{Mo}_3\text{S}_{13}]^{2-}$  cluster on BiOBr possesses a plenty of active sites as the photogenerated electron capture center and promotes the charge separation [28]. However, overloading of these brown  $[\text{Mo}_3\text{S}_{13}]^{2-}$  clusters (6.5 wt%  $\text{Mo}_3\text{S}_{13}^{2-}/\text{BiOBr}$ ) could block the light absorbance for BiOBr catalyst [40,41].

The photoinduced holes or the formed radicals ( $\bullet\text{OH}$  and  $\bullet\text{O}_2^-$ ) are the two main species for the oxidization of organic pollutants. In order to explore the possible mechanisms involved in RhB photodecolorization over the  $\text{Mo}_3\text{S}_{13}^{2-}/\text{BiOBr}$  sample, EDTA-2Na and *tert*-butanol (TBA) was used as a hole scavenger and a hydroxyl radical scavenger ( $\bullet\text{OH}$ ) respectively [42,43]. In addition, the formation of superoxide radical ( $\bullet\text{O}_2^-$ ) could be inhibited by removal of  $\text{O}_2$  via purging Ar in the catalytic system. It turned out that the decolorization of RhB was significantly inhibited in the presence of EDTA-2Na, which indicated that the photogenerated holes were the main oxidative species in  $\text{Mo}_3\text{S}_{13}^{2-}/\text{BiOBr}$  composite (Fig. 5(b)). Simultaneously, the photogenerated electrons could easily migrate from the inner region to the surface to participate in the surface reaction to form active radicals ( $\bullet\text{OH}$  and  $\bullet\text{O}_2^-$ ). The surface-adsorbed  $\text{O}_2$  as an electron acceptor could react with electrons to generate  $\bullet\text{O}_2^-$  which could further transform to  $\bullet\text{OH}$  via a series of reactions with  $\text{H}^+$ . In the absence of  $\text{O}_2$ , most electrons recombined with holes. Therefore, the photocatalytic activity of the  $\text{Mo}_3\text{S}_{13}^{2-}/\text{BiOBr}$  composite was greatly decreased without  $\text{O}_2$  as shown in Fig. 5(b). Thus, it was believed that the decolorization of RhB over  $\text{Mo}_3\text{S}_{13}^{2-}/\text{BiOBr}$  composite was dominated by the direct hole and the generated  $\bullet\text{O}_2^-$  radicals oxidation process. These results suggest that the deposited  $[\text{Mo}_3\text{S}_{13}]^{2-}$  clusters can act as electron traps to facilitate the photogenerated electron/hole separation for BiOBr composite [44–49]. The photogenerated electrons are trapped by  $\text{O}_2$  to form active oxygen species like  $\bullet\text{O}_2^-$  which could effectively oxidize RhB. On the other hand, photogenerated holes not only directly decompose the organic compounds but also accumulate at the valence band (VB) of BiOBr to react with  $\text{H}_2\text{O}$  to form hydroxyl radical  $\bullet\text{OH}$ , which is the photo-oxidation process. In addition, the amount of  $[\text{Mo}_3\text{S}_{13}]^{2-}$  clusters also influence the efficiency of electron–hole separation. The incorporation of  $[\text{Mo}_3\text{S}_{13}]^{2-}$  clusters onto BiOBr could significantly improve the photocatalytic activity and the optimal content of  $[\text{Mo}_3\text{S}_{13}]^{2-}$  clusters is found to be around 5 wt%. The larger amount of  $[\text{Mo}_3\text{S}_{13}]^{2-}$  clusters form overlapping agglomerates and smother the surface, which cause the loss of surface area and inhibit the light absorption of pure BiOBr.

Photocatalytic activities of BiOX (X = Cl, Br and I) could be dramatically improved by depositing precious metals such as Pt and Pd [50].  $[\text{Mo}_3\text{S}_{13}]^{2-}$  clusters have been demonstrated to be an



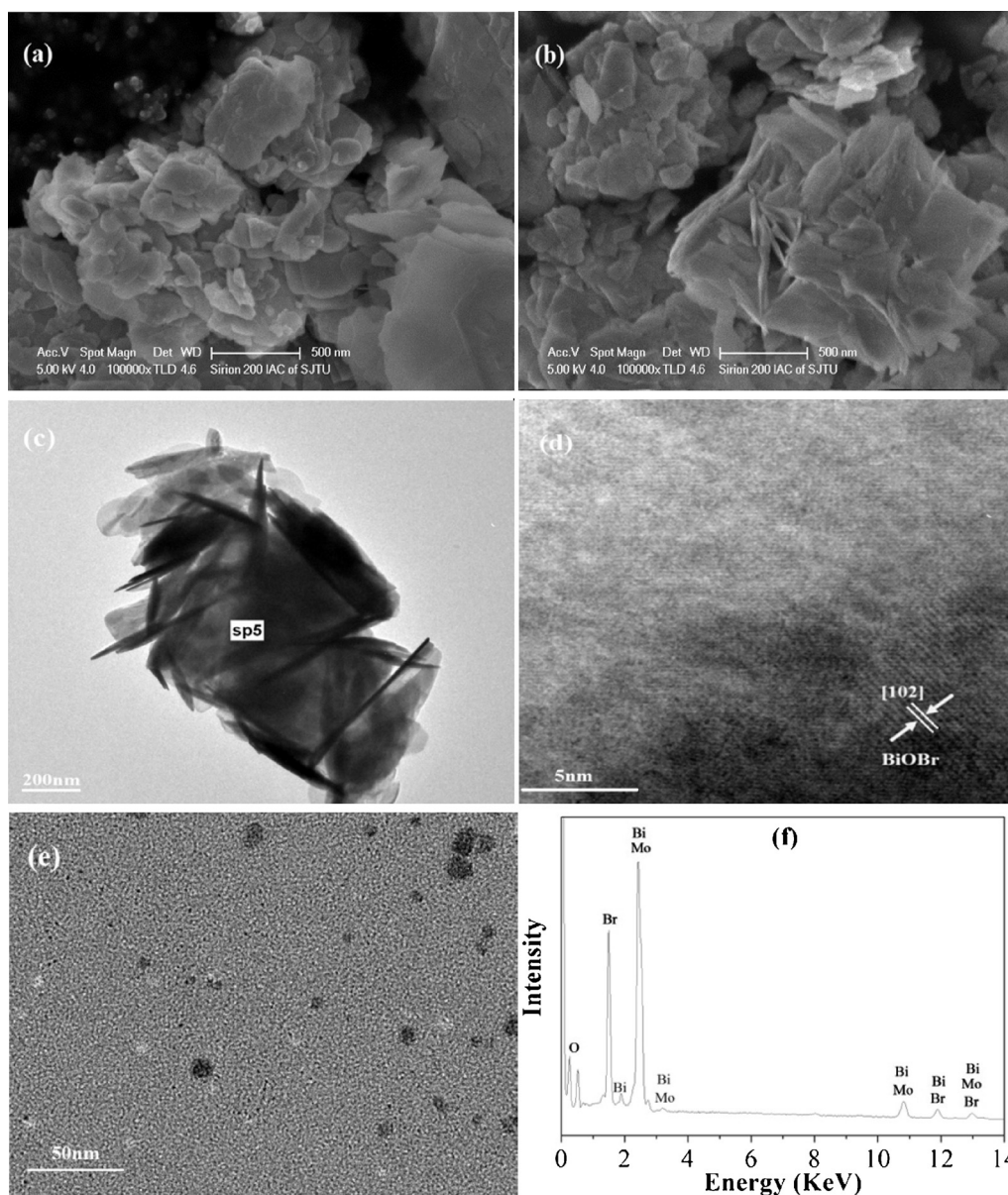


**Fig. 2.** SEM images of pure BiOBr (a) and 5 wt%  $\text{Mo}_3\text{S}_{13}^{2-}/\text{BiOBr}$  composite (b); TEM images of 5 wt%  $\text{Mo}_3\text{S}_{13}^{2-}/\text{BiOBr}$  composite (c) and  $(\text{NH}_4)_2\text{Mo}_3\text{S}_{13} \cdot n\text{H}_2\text{O}$  clusters (d); HRTEM image of 5 wt%  $\text{Mo}_3\text{S}_{13}^{2-}/\text{BiOBr}$  composite (e); EDS of 5 wt%  $\text{Mo}_3\text{S}_{13}^{2-}/\text{BiOBr}$  composite recorded on the square in Fig. 2(c) (f).

“platinum-like” catalyst for electrolysis [28]. As revealed in Fig. 6, 1 wt% Pt/ $\text{TiO}_2$  and 5 wt%  $\text{Mo}_3\text{S}_{13}^{2-}/\text{TiO}_2$  showed the comparable activities on photocatalytic decolorization of RhB under the irradiation of UV light. Our 5 wt%  $\text{Mo}_3\text{S}_{13}^{2-}/\text{BiOBr}$  composite has the similar photocatalytic performance for decolorization of RhB as the 1 wt% Pt/BiOBr under the visible light irradiation. The resistance of the catalyst toward sulfur poisoning is an important aspect of the photocatalysis processes and sulfur compounds are the most serious poison for Pt catalysts. It is well known that the activity of supported platinum catalysts could be easily poisoned by traces of S [51]. It has been recently shown that in aqueous systems, the formation of bulk PtS may occur besides surface Pt-S interaction. During sulfur poisoning,  $\text{S}^{2-}$  is absorbed onto the Pt/BiOBr composites or Pt/ $\text{TiO}_2$  composites. The adsorbed  $\text{S}^{2-}$  could diffuse to the Pt/BiOBr composites or Pt/ $\text{TiO}_2$  composites interface and react with Pt to form platinum sulfides, which result in a loss of photocatalytic activities [52]. In the sulfur free condition, 5 wt%  $\text{Mo}_3\text{S}_{13}^{2-}/\text{BiOBr}$  composite and 1 wt% Pt/BiOBr composite exhibit the similar activity on photocatalytic decolorization of RhB (Fig. 6).

In the presence of  $\text{S}^{2-}$ , the photocatalytic decolorization of RhB on 5 wt%  $\text{Mo}_3\text{S}_{13}^{2-}/\text{BiOBr}$  composite, pure BiOBr and 1 wt% Pt/BiOBr composite were suppressed in the beginning 90 min, 150 min and 150 min, respectively, owing to the oxidation of  $\text{S}^{2-}$ . After oxidation of the  $\text{S}^{2-}$ , 1 wt% Pt/BiOBr composite has the similar activities on the removal of RhB as the pure BiOBr, which suggests that the Pt co-catalyst on the Pt/BiOBr composite have lost its function of promoting the electron-hole separation due to the Pt sulfur poisoning. However, more than 90% of RhB could be removed by 5 wt%  $\text{Mo}_3\text{S}_{13}^{2-}/\text{BiOBr}$  composite within 60 min, suggesting its resistance to sulfur poisoning. To demonstrate the advantage of  $[\text{Mo}_3\text{S}_{13}]^{2-}$  cluster as co-catalyst for photocatalysts, the sulfur tolerance of  $\text{Mo}_3\text{S}_{13}^{2-}/\text{BiOBr}$  composite has also been tested by the decolorization of sulfur-containing dye such as methylene blue (MB) under visible light irradiation. As indicated in Figs. S4 and S5, 5 wt%  $\text{Mo}_3\text{S}_{13}^{2-}/\text{BiOBr}$  composites showed the best photocatalytic performance than others. After 180 min irradiation, the MB solution was almost completely decolorized by 5 wt% BiOBr/ $\text{Mo}_3\text{S}_{13}$ . The above results further confirmed that  $\text{Mo}_3\text{S}_{13}^{2-}/\text{BiOBr}$  compos-

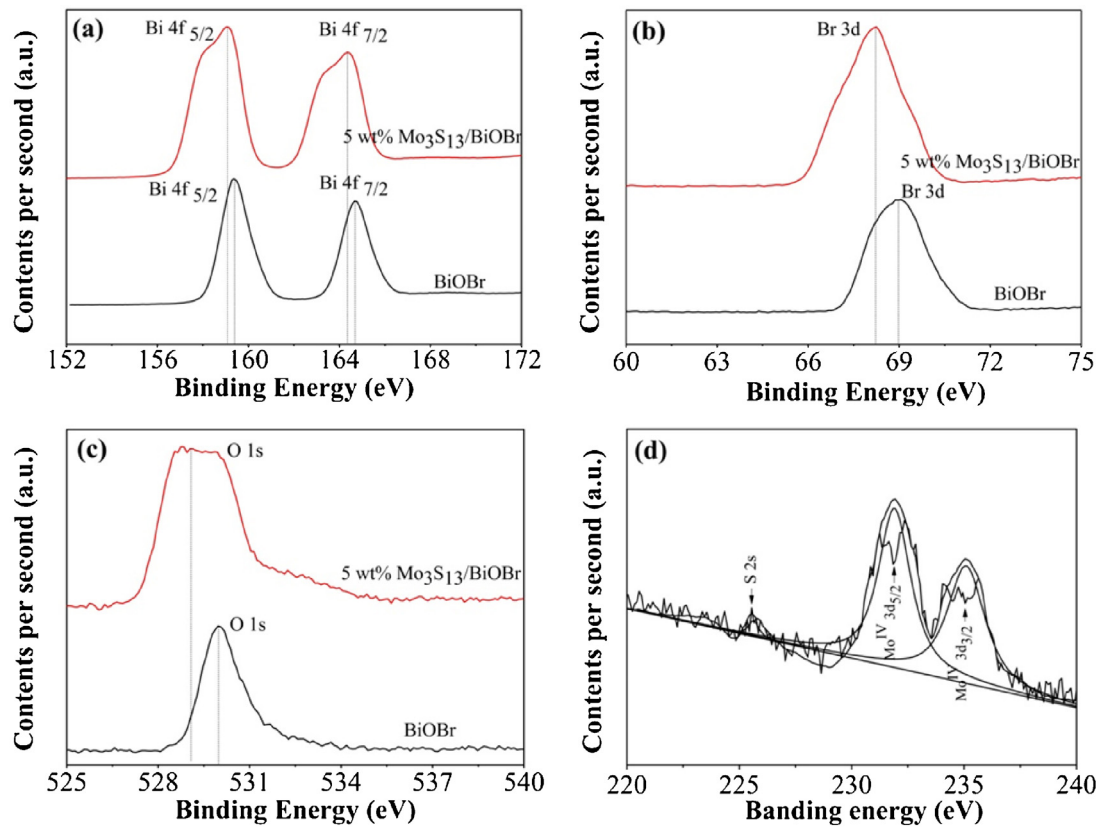


Fig. 3. High resolution XPS spectra for 5 wt%  $\text{Mo}_3\text{S}_{13}^{2-}/\text{BiOBr}$  composite. (a) Bi 4f; (b) O 1s; (c) Br 3d; and (d) Mo 3d and S 2s of the  $\text{Mo}_3\text{S}_{13}^{2-}/\text{BiOBr}$  composite.

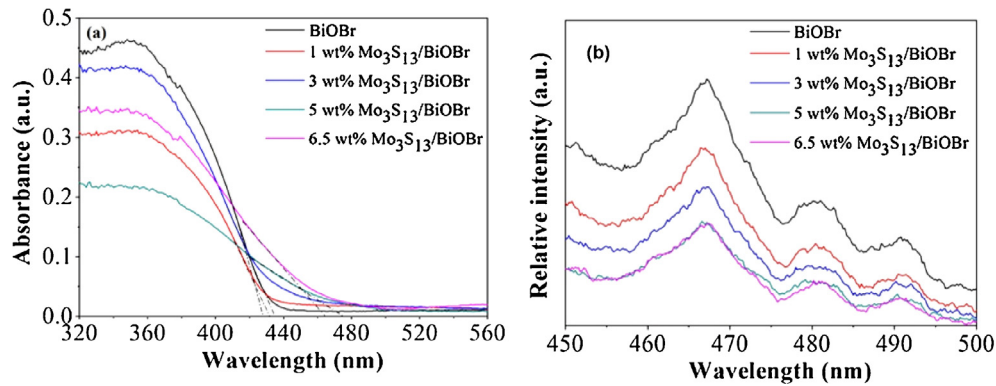


Fig. 4. (a) UV-vis diffuse reflectance spectra and (b) PL spectra of pure BiOBr and  $\text{Mo}_3\text{S}_{13}^{2-}/\text{BiOBr}$  composites with different  $[\text{Mo}_3\text{S}_{13}]^{2-}$  contents.

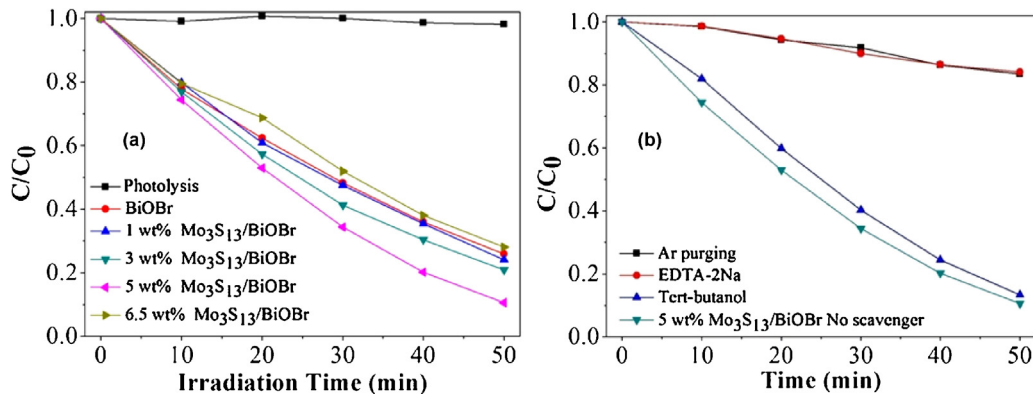
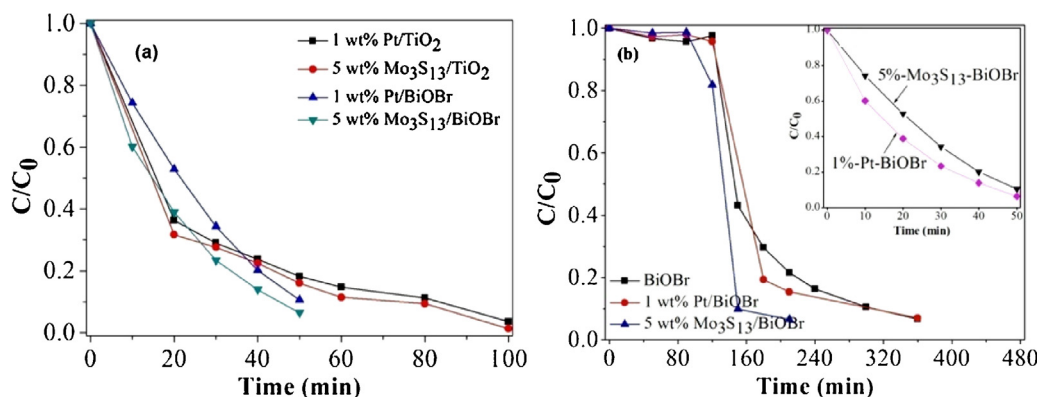
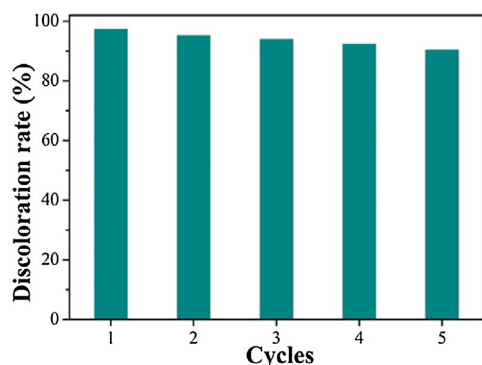


Fig. 5. (a) Photocatalytic efficiency of RhB decolorization for pure BiOBr and  $\text{Mo}_3\text{S}_{13}^{2-}/\text{BiOBr}$  composites with different  $[\text{Mo}_3\text{S}_{13}]^{2-}$  contents. (b) Comparison of photocatalytic activities of 5 wt%  $\text{Mo}_3\text{S}_{13}^{2-}/\text{BiOBr}$  catalyst for the decolorization of RhB with or without Ar purging, adding EDTA-2Na and *t*-butanol under visible light irradiation.



**Fig. 6.** (a) Comparison of photocatalytic activities for the decolorization of RhB by 1 wt% Pt/TiO<sub>2</sub> and 5 wt% Mo<sub>3</sub>S<sub>13</sub><sup>2-</sup>/TiO<sub>2</sub> under UV light irradiation and 5 wt% Mo<sub>3</sub>S<sub>13</sub><sup>2-</sup>/BiOBr composite and 1 wt% Pt/BiOBr composite under visible light irradiation. (b) Photocatalytic activities of RhB decolorization under visible light irradiation for 1 wt% Pt/BiOBr catalyst and 5 wt% Mo<sub>3</sub>S<sub>13</sub><sup>2-</sup>/BiOBr catalyst without and with sulfur.



**Fig. 7.** Cycling runs of photocatalytic degradation of MB using the 5 wt% Mo<sub>3</sub>S<sub>13</sub><sup>2-</sup>/BiOBr composite under visible light irradiation.

ite photocatalysts possessed excellent photocatalytic activity and sulfur tolerance. Furthermore, the cycling runs of the MB decolorization by 5.0 wt% Mo<sub>3</sub>S<sub>13</sub><sup>2-</sup>/BiOBr composites were carried out to evaluate its photocatalytic stability and recyclability, especially for the co-catalysts of Mo<sub>3</sub>S<sub>13</sub><sup>2-</sup>. As illustrated in Fig. 7, the Mo<sub>3</sub>S<sub>13</sub><sup>2-</sup>/BiOBr composites exhibited only little decrease in photocatalytic activities after five cycles of photocatalytic decolorization MB. These results suggest that Mo<sub>3</sub>S<sub>13</sub><sup>2-</sup>/BiOBr composites is a promising potential stable photocatalyst candidate for photocatalytic applications.

#### 4. Conclusion

In summary, a highly photocatalytic active Mo<sub>3</sub>S<sub>13</sub><sup>2-</sup>/BiOBr nanocomposite were prepared via a facile hydrothermal synthesis. The low cost and earth abundant [Mo<sub>3</sub>S<sub>13</sub>]<sup>2-</sup> clusters (~15 nm) were successfully deposited on the surface of BiOBr microspheres. This novel nanocomposite exhibited an admirable photocatalytic activity comparable to state of art Pt/BiOBr photocatalyst. The enhanced visible light photocatalytic activity of Mo<sub>3</sub>S<sub>13</sub><sup>2-</sup>/BiOBr composites mainly contributed to the co-catalysts of [Mo<sub>3</sub>S<sub>13</sub>]<sup>2-</sup> clusters, which effective promote the photoinduced charges transfer and separation. The results indicated that [Mo<sub>3</sub>S<sub>13</sub>]<sup>2-</sup> cluster is a promising Pt alternative co-catalyst for photocatalyst. Furthermore, our Mo<sub>3</sub>S<sub>13</sub><sup>2-</sup>/BiOBr nanocomposite shows enhanced sulfur tolerant photocatalytic activities while the Pt/BiOBr would be total deactivated by Pt's sulfur poison. In all, the low cost, highly photocatalytic active, excellent photocatalytic stability and recyclability of Mo<sub>3</sub>S<sub>13</sub><sup>2-</sup>/BiOBr nanocomposite enable it to be a promising

candidate for the environmental remediation on sulfur containing water pollutant.

#### Acknowledgements

This worked is financial supported by Recruitment Program of Global Experts in China, the start-up funds from Shanghai Jiao Tong University, NSFC (Grant 51372151, 21303103) and the Foundation of Shanghai Government (15PJ1404000).

#### Appendix A. Supplementary data

Supplementary data associated with this article can be found, in the online version, at <http://dx.doi.org/10.1016/j.apcatb.2015.10.020>.

#### References

- [1] X. Chen, S. Shen, L. Guo, S.S. Mao, Chem. Rev. 110 (2010) 6503–6570.
- [2] X. Hu, G. Li, J.C. Yu, Langmuir: ACS J. Surf. Colloids 26 (2010) 3031–3039.
- [3] J. Jiang, L. Zhang, H. Li, W. He, J.J. Yin, Nanoscale (2013) 10573–10581.
- [4] Y. Feng, L. Li, J. Li, J. Wang, L. Liu, J. Hazard. Mater. 192 (2011) 538–544.
- [5] L. Ye, J. Liu, Z. Jiang, T. Peng, L. Zan, Appl. Catal. B 142 (2013) 1–7.
- [6] J. Xu, W. Meng, Y. Zhang, L. Li, C. Guo, Appl. Catal. B 107 (2011) 355–362.
- [7] L. Ye, C. Gong, J. Liu, L. Tian, T. Peng, K. Deng, L. Zan, J. Mater. Chem. 22 (2012) 8354.
- [8] J. Xia, J. Di, S. Yin, H. Xu, J. Zhang, Y. Xu, L. Xu, H. Li, M. Ji, RSC Adv. 4 (2014) 82–90.
- [9] J. Henle, P. Simon, A. Frenzel, S. Scholz, S. Kaskel, Chem. Mater. 19 (2007) 366–373.
- [10] L. Ye, J. Liu, C. Gong, L. Tian, T. Peng, L. Zan, ACS Catal. 2 (2012) 1677–1683.
- [11] X. Zhang, Z. Ai, F. Jia, L. Zhang, J. Phys. Chem. C 112 (2008) 747–753.
- [12] F. Yanfen, H. Yingping, Y. Jing, W. Pan, C. Genwei, Environ. Sci. Technol. 45 (2011) 1593–1600.
- [13] J. Xia, S. Yin, H. Li, H. Xu, Y. Yan, Q. Zhang, Langmuir: ACS J. Surf. Colloids 27 (2010) 1200–1206.
- [14] J. Xiong, G. Cheng, F. Qin, R. Wang, H. Sun, R. Chen, Chem. Eng. J. 220 (2013) 228–236.
- [15] J. Xia, J. Di, S. Yin, H. Xu, J. Zhang, Y. Xu, L. Xu, H. Li, M. Ji, RSC Adv. 4 (2014) 82–90.
- [16] W.L. Huang, Q. Zhu, Comput. Mater. Sci. 43 (2008) 1101–1108.
- [17] L. Ye, L. Zan, L. Tian, T. Peng, J. Zhang, Chem. Commun. 47 (2011) 6951–6953.
- [18] L. Zhang, X.F. Cao, X.T. Chen, Z.L. Xue, J. Colloid Interface Sci. 354 (2011) 630–636.
- [19] D. Zhang, Y. Guo, Intelligent Science and Intelligent Data Engineering, Springer, 2012, pp. 104–111.
- [20] H. Cheng, B. Huang, Y. Dai, Nanoscale 6 (2014) 2009–2026.
- [21] L. Ye, Y. Su, X. Jin, H. Xie, C. Zhang, Environ. Sci. Nano 1 (2014) 90–112.
- [22] D. Zhang, J. Li, Q. Wang, Q. Wu, J. Mater. Chem. A 1 (2013) 8622–8629.
- [23] J.J. Zhong, Q.Y. Meng, B. Liu, X.B. Li, X.W. Gao, T. Lei, C.J. Wu, Z.J. Li, C.H. Tung, L.Z. Wu, Org. Lett. 16 (2014) 1988–1991.
- [24] X. Zhang, Z. Ai, F. Jia, L. Zhang, J. Phys. Chem. C 112 (2008) 747–753.
- [25] Y. Huo, J. Zhang, M. Miao, Y. Jin, Appl. Catal. B 111 (2012) 334–341.
- [26] D. Zhang, M. Wen, B. Jiang, G. Li, J.C. Yu, J. Hazard. Mater. 211–212 (2012) 104–111.
- [27] J. Xia, S. Yin, H. Li, H. Xu, L. Xu, Y. Xu, Dalton Trans. 40 (2011) 5249–5258.

- [28] J. Kibsgaard, T.F. Jaramillo, F. Besenbacher, *Nat. Chem.* 6 (2014) 248–253.
- [29] D. Recatalá, R. Llusar, A.L. Gushchin, E.A. Kozlova, Y.A. Laricheva, P.A. Abramov, M.N. Sokolov, R. Gómez, T. Lana-Villarreal, *Chem. Sus. Chem.* 8 (2015) 148–157.
- [30] T. Weber, J. Muijsers, J. Niemantsverdriet, *J. Phys. Chem.* 99 (1995) 9194–9200.
- [31] A. Leist, S. Stauf, S. Löken, E.W. Finckh, S. Lüdtke, K.K. Unger, W. Assenmacher, W. Mader, W. Tremel, *J. Mater. Chem.* 8 (1998) 241–244.
- [32] T.F. Jaramillo, J. Bonde, J. Zhang, B.-L. Ooi, K. Andersson, J. Ulstrup, I. Chorkendorff, *J. Phys. Chem. C* 112 (2008) 17492–17498.
- [33] H. Zhang, Y. Yang, Z. Zhou, Y. Zhao, L. Liu, *J. Phys. Chem. C* 118 (2014) 14662–14669.
- [34] A. Falch, R.J. Kriek, *J. Photochem. Photobiol. A: Chem.* 271 (2013) 117–123.
- [35] H. Zhang, Y. Yang, Z. Zhou, Y. Zhao, L. Liu, *J. Phys. Chem. C* 118 (2014) 14662–14669.
- [36] A. Müller, V. Wittneben, E. Krickemeyer, H. Bögge, M. Lemke, Z. Anorg. Allg. Chem. 605 (1991) 175–188.
- [37] Y. Hou, A.B. Laursen, J. Zhang, G. Zhang, Y. Zhu, X. Wang, S. Dahl, I. Chorkendorff, *Angew. Chem. Int. Ed.* 52 (2013) 3621–3625.
- [38] L. Ge, C. Han, X. Xiao, L. Guo, *Int. J. Hydrogen Energy* 38 (2013) 6960–6969.
- [39] J. Di, J. Xia, Y. Ge, L. Xu, H. Xu, J. Chen, M. He, H. Li, *Dalton Trans.* 43 (2014) 15429–15438.
- [40] Y. Wang, R. Shi, J. Lin, Y. Zhu, *Energy Environ. Sci.* 4 (2011) 2922–2929.
- [41] J. Fu, Y. Tian, B. Chang, F. Xi, X. Dong, *J. Mater. Chem.* 22 (2012) 21159–21166.
- [42] X. Li, N. Kikugawa, J. Ye, *Adv. Mater.* 20 (2008) 3816–3819.
- [43] H. Lee, W. Choi, *Environ. Sci. Technol.* 36 (2002) 3872–3878.
- [44] S. Hwang, M.C. Lee, W. Choi, *Appl. Catal. B* 46 (2003) 49–63.
- [45] C. YiHung, C. LiLin, S. NengChou, *J. Hazard. Mater.* 172 (2009) 20–29.
- [46] D. Hufschmidt, D. Bahnemann, J.J. Testa, C.A. Emilio, M.I. Litter, *J. Photochem. Photobiol. A* 148 (2002) 223–231.
- [47] A. Yamakata, T.-A. Ishibashi, H. Onishi, *J. Photochem. Photobiol. B* 105 (2001) 7258–7262.
- [48] Y.K. Choi, S.S. Seo, K.H. Chjo, Q.W. Choi, S.M. Park, *J. Electrochem. Soc.* 139 (1992) 1803–1807.
- [49] A. Furube, T. Asahi, H. Masuhara, H. Yamashita, M. Anpo, *Chem. Phys. Lett.* 336 (2001) 424–430.
- [50] C. Yu, F. Cao, G. Li, R. Wei, J.C. Yu, R. Jin, Q. Fan, C. Wang, *Sep. Purif. Technol.* 120 (2013) 110–122.
- [51] A. Melchor, E. Garbowski, M. Mathieu, M. Primet, *React. Kinet. Catal. Lett.* 29 (1985) 371–377.
- [52] J.-F. Chiou, Y.-L. Huang, T.-B. Lin, J.-R. Chang, *Ind. Eng. Chem. Res.* 34 (1995) 4277–4283.